Luminous mid-IR selected obscured quasars at cosmic noon in SDSS Stripe82 II: spectroscopic diversity and broad Hα emissions

Wang, B.; Ishikawa, Y.; Hennawi, J.F.; Cai, Z.; Richards, G.T.; Zakamska, N.L.; ... ; Schindler, J.-T.

Monthly Notices of the ROYAL ASTRONOMICAL SOCIETY

MNRAS **544,** 687–707 (2025) https://doi.org/10.1093/mnras/staf1730
Advance Access publication 2025 October 10

Luminous mid-IR selected obscured quasars at cosmic noon in SDSS Stripe82 II: spectroscopic diversity and broad H α emissions

Ben Wang [1,2★] Yuzo Ishikawa,[3] Joseph F. Hennawi [2,4] Zheng Cai,[1] Gordon T. Richards,[5] Nadia L. Zakamska [6,7] Daming Yang[2] and Jan-Torge Schindler[8]

[1]*Department of Astronomy, Tsinghua University, Beijing 100084, China*
[2]*Leiden Observatory, Leiden University, Leiden NL-2333 CA, the Netherland*
[3]*MIT Kavli Institute for Astrophysics and Space Research, Massachusetts Institute of Technology, Cambridge, MA 02139, USA*
[4]*Department of Physics, Broida Hall, University of California, Santa Barbara, CA 93106-9530, USA*
[5]*Department of Physics, Drexel University, 32 S. 32nd Street, Philadelphia, PA 19104, USA*
[6]*Department of Physics and Astronomy, Bloomberg Center, Johns Hopkins University, Baltimore, MD 21218, USA*
[7]*Institute for Advanced Study, Princeton University, Princeton, NJ 08544, USA*
[8]*Hamburg Observatory, University of Hamburg, Gojenbergsweg 112, D-21029 Hamburg, Germany*

Accepted 2025 September 25. Received 2025 September 23; in original form 2025 August 1

ABSTRACT

We present a multiwavelength spectroscopic survey of 23 luminous mid-infrared-selected Type-2 quasars at the redshifts of $z = 0.88$–3.49. The targets were selected in the SDSS Stripe 82 field based on their bright WISE 22 μm detections and extremely faint or red optical counterparts. Near-infrared (Gemini/Gemini Near-InfraRed Spectrograph) and optical (Keck/Low Resolution Imaging Spectrometer and Keck Cosmic Web Imager Integral Field Spectrograph) spectroscopy confirm 23 out of 24 candidates as Type-2 quasars, including 12 objects at $z > 2$. The spectra exhibit strong rest-frame UV and optical emission lines (Ly α, C IV, [O III], H α) with a wide range of line widths, indicating significant spectral diversity. Approximately one-third of the sample (8 of 23) shows broad H α emission (full width at half-maximum, FWHM$> 2000\,\mathrm{km\,s^{-1}}$) despite their Type-2 classification, while the rest have only narrow lines (FWHM $< 2000\,\mathrm{km\,s^{-1}}$) characteristic of classical obscured quasars. Notably, these broad-line Type-2 quasars share similar spectral energy distributions with the *James Webb Space Telescope* (*JWST*)-discovered 'little red dot', suggesting that our sample could be lower redshift analogues of the heavily obscured broad-line AGNs uncovered by *JWST*. We also find that the [O III] λ5007 emission is relatively weak for their high-bolometric luminosities, deviating from trends seen in lower-z Type-2 quasi-stellar objects (QSOs). A new composite spectrum for Type-2 QSOs is built using our sample. Overall, our results demonstrate that mid-infrared selection efficiently uncovers diverse populations of obscured quasars and that spectroscopic follow-up is crucial for revealing their true nature. This study provides new insights into heavily obscured supermassive black hole growth at cosmic noon and bridges the gap to the obscured active galactic nuclei populations being revealed by *JWST*.

Key words: galaxies: high-redshift – quasars: emission lines – quasars: general – quasars: supermassive black holes – infrared: galaxies.

1 INTRODUCTION

Quasars, or quasi-stellar objects (QSOs), are among the most luminous objects in the universe, powered by accretion on to supermassive black holes (SMBHs) at their centres (M. Schmidt 1963). Their intense radiation originates from the accretion of matter on to the SMBH, producing high-energy emission across multiple wavelengths. According to the classical 'unified' model (R. Antonucci 1993; C. M. Urry & P. Padovani 1995) for active galactic nuclei (AGN), there are two different types of AGNs. In Type-1, or unobscured, AGNs, both continuum emission from the accretion disc region and broad emission lines from the broad-line region can be detected. The other type are called Type-2, or obscured, AGN. In this case, the line of sight to the broad emission line and the central continuum regions are obscured by the dusty torus, so only the narrow emission lines can be detected. The definition of Type-2 QSOs or obscured QSOs varies in different papers. In this paper, we use Type-2 QSOs to describe all types of obscured QSOs. In the classical 'unified' model, the viewing angle is the main reason to cause the difference of these two types of AGNs. Another scenario is that the difference between Type-1 and Type-2 QSOs is due to evolutionary effects. In this picture, Type-1 and Type-2 QSOs reflect different evolutionary phases, especially after galaxy mergers (e.g. D. B. Sanders et al. 1988; P. F. Hopkins et al. 2006). Some researchers even find that the environment around Type-2 AGNs could be denser than Type-1 AGNs (Z. Cai et al. 2017; S. Zhang et al. 2023). Investigating the relative abundances of of Type-1 and Type-2 QSOs across cosmic time can help us to better understand the physical processes producing these two different kinds of QSOs,

★ E-mail: bwang@mail.strw.leidenuniv.nl

and further understand the SMBH accretion and SMBH/galaxy co-evolution.

In the past decades, large-scale surveys have discovered substantial numbers of Type-1 QSOs, with more than 750 000 identified through dedicated programmes such as the Sloan Digital Sky Survey (SDSS; e.g. D. P. Schneider et al. 2007; B. W. Lyke et al. 2020) and the ongoing Dark Energy Spectroscopic Instrument (DESI) survey (e.g. E. Chaussidon et al. 2023; DESI Collaboration 2024). Dedicated efforts have pushed the Type-1 QSO frontier to $z > 7$ (e.g. E. Bañados et al. 2018; F. Wang et al. 2021). For Type-2 QSOs, dust obscuration makes them faint in the ultraviolet (UV)/optical; thus, multiwavelength data are needed to isolate these objects. Sizable samples of Type-2 QSOs have been identified from mid-infrared (mid-IR), X-ray, and the SDSS prior to the launch of *James Webb Space Telescope* (*JWST*; e.g. N. L. Zakamska & others 2003; M. Haas et al. 2004; A. Alonso-Herrero et al. 2006; A. Martínez-Sansigre et al. 2006; K. Brand et al. 2007; R. Alexandroff et al. 2013; M. Lacy et al. 2013; S. Yuan, M. A. Strauss & N. L. Zakamska 2016). However, the majority of these Type-2 quasars are low-luminosity objects at $z < 1$. The number of spectroscopically confirmed luminous Type-2 QSO at $z > 2$ is still very limited (M. Lacy et al. 2013), leading to a poorly understood QSO luminosity function for obscured QSO populations (E. Glikman et al. 2018). Some low-z Type-2 QSO surveys suggest that there should be an intrinsically large obscured population at high-z, and their number density is comparable to the unobscured population (e.g. A. Martínez-Sansigre et al. 2005; R. J. Assef et al. 2015; M. Lacy et al. 2015). However, such a large obscured population was not widely observationally identified using ground-based facilities.

The identification of obscured quasars relies on multiwavelength selection techniques combined with spectroscopic confirmation. Optical Type-2 QSO samples from SDSS spectroscopy represent the most extensive collections at low redshifts $z < 1$ (N. L. Zakamska et al. 2003, 2006; R. Reyes et al. 2008; S. Yuan et al. 2016). X-ray surveys offer an alternative method to uncover Type-2 AGN (M. d. C. Polletta et al. 2006; W. N. Brandt & D. M. Alexander 2015; A. Peca et al. 2023, 2024); however, these surveys often depend on uncertain or poorly calibrated photometric redshifts and X-ray surveys will miss Compton-thick objects with high-photoelectric obscuring columns $N_{\rm H} > 10^{24}\,{\rm cm}^{-2}$.

Nevertheless, previous multiwavelength surveys of Type-2 quasars have assembled substantial samples that allow measurements of the obscured-to-unobscured quasar ratio (Type-2:Type-1) at $z \lesssim 2$. According to the AGN unification model, the number density of Type-1 and Type-2 QSOs should be comparable through cosmic time, both peaking at $z \sim 2.5$ (G. T. Richards et al. 2006; N. P. Ross et al. 2013). Decades of AGN/QSO censuses across the electromagnetic spectrum (e.g. N. L. Zakamska et al. 2003; R. J. Assef et al. 2013; M. Lacy et al. 2013; L. Yan et al. 2013; W. N. Brandt & D. M. Alexander 2015) have led to the consensus that the Type-2:Type-1 ratio is comparable at low redshift $z < 1$ (e.g. R. Reyes et al. 2008; A. Lawrence & M. Elvis 2010; A. Merloni et al. 2014), consistent with the unification models.

However, recent *JWST* observations suggest the presence of a previously undetected, substantial population of potentially obscured AGN at high redshift ($4 \lesssim z \lesssim 9$), often referred to as 'little red dots' (LRDs; e.g. J. E. Greene et al. 2024; D. D. Kocevski et al. 2023; J. Matthee et al. 2024). Some of these sources show broad emission lines in their spectra, suggestive of active accretion on to a supermassive black hole (e.g. Y. Harikane et al. 2023; V. Kokorev et al. 2023). Intriguingly, the inferred obscured-to-unobscured ratio from these *JWST* detections is possibly as extreme as $\sim 10^{3-4} : 1$ (E. Pizzati et al. 2024), far exceeding expectations from previous models. Following the Sołtan argument (A. Soltan 1982), this would suggest as much SMBH growth at $z \gtrsim 4$ as at later times (K. Inayoshi 2025). But the redshift distribution of these LRDs is mainly at $z = 4 - 9$ (e.g. H. B. Akins et al. 2025). It remains uncertain whether a similarly large obscured population exists at intermediate redshifts at $2 < z < 4$. This gap introduces substantial uncertainty in our understanding of the cosmic history of SMBH growth and the full evolution of the quasar population.

Identifying the obscured QSO population at intermediate redshift $2 < z < 4$ is the key to bridging this gap. Mid-IR selection provides a more complete and less biased approach to identifying obscured quasars. Colour-selection criteria, such as mid-IR colour wedges defined using *Spitzer* (M. Lacy et al. 2004; D. Stern et al. 2005; M. Polletta et al. 2008; J. L. Donley et al. 2012) and later the Wide-field Infrared Survey Explorer (WISE) (R. J. Assef et al. 2013; E. Glikman et al. 2018; C. Andonie et al. 2025) have been used to select AGN candidates that are subsequently confirmed via optical and IR spectroscopy (M. Lacy et al. 2013; E. Glikman et al. 2018). However, the redshift distribution of mid-IR-selected Type-2 quasars shows a sharp decline beyond $z > 1$, with only 18 spectroscopically confirmed luminous Type-2 QSOs known at $z > 2$ in M. Lacy et al. (2013).

A very simple selection requiring a red optical to mid-IR $r - [24\,\mu{\rm m}] \gtrsim 8$ colour (AB), has been shown to efficiently identify $z \gtrsim 2$ dust obscured galaxies (DOGs; K. Brand et al. 2007; A. Dey et al. 2008; L. Yan et al. 2013). The effectiveness of DOG selection is intuitive: adopting the reddest possible mid-IR band probes the peak of the AGN IR spectral energy distribution (SED; $\lambda_{\rm rest} \sim 10\,\mu{\rm m}$), while demanding a red $r - [24\,\mu{\rm m}]$ colour excludes objects with AGN emission at bluer wavelengths. The DOG selection uncovers a large population of the obscured populations with all diversity, and the number density $\sim 0.9\,{\rm deg}^{-2}$ is comparable to the Type-1 QSO population with the same W4 flux level (L. Yan et al. 2013).

A notable subset of WISE-selected AGNs are the so-called W1W2 dropouts or Hot Dust Obscured Galaxies (Hot DOGs), characterized by extremely red mid-IR spectral energy distributions. Published spectra of ~ 60 Hot DOGs indicate that ~ 40 are type-2s at $z \gtrsim 2$ (J. Wu et al. 2012; C.-W. Tsai et al. 2015). However, these objects are nearly an order of magnitude less abundant in the sky (252 Hot-DOGs in 32 000 deg^2, P. R. M. Eisenhardt et al. 2012; R. J. Assef et al. 2015) than DOGs, implying that they likely constitute the (mid-IR) reddest subset of the Type-2 population. Most WISE-selected obscured quasars are still located at $z < 2$, and their number density is well below Type-1 QSOs. Some extremely red quasars (ERQs) and heavily reddened quasars are also selected using the IR selection (e.g. M. Banerji et al. 2015; N. P. Ross et al. 2015; N. L. Zakamska et al. 2016; F. Hamann et al. 2017; R. M. Alexandroff et al. 2018; M. J. Temple et al. 2019; N. L. Zakamska & R. M. Alexandroff 2023). However, these samples often include optical magnitude cuts like $i < 20.5$, introducing significant luminosity biases and making them a subset of the whole obscured population.

In this project, we present spectroscopic observations of a sample of obscured QSOs at $z \sim 2$ (Y. Ishikawa et al. 2023; B. Wang et al. 2025), using the DOG selection in the SDSS Stripe82 region. The sample selection and the Gemini/Gemini Near-InfraRed Spectrograph (GNIRS) spectra for a subsample are stated in Y. Ishikawa et al. (2023). The SED fitting and composite photometry are described in B. Wang et al. (2025). In this paper, we show the new Keck and Gemini observations for the whole sample. The spectra of these targets are obtained with state-of-the-art ground-based optical and near-infrared telescopes: Keck and Gemini. These 24 candidates are selected using a red colour selection ($r - W4 > 8.38$).

Gemini/GNIRS is used for identifying the 24 targets, 20 of which are further observed with Keck to better constrain the redshift and reveal the rest-UV spectra. The SED fitting of this sample reveals that the IR emission is dominated by the hot dust torus, and the rest-UV/optical is the combination of the AGN and galaxy emission (B. Wang et al. 2025). This paper is divided as follows: In Section 2, we introduce the target selection, observation, and data reduction. In Section 3, we conduct the emission line fitting, discuss the line property, and spectral diversity based on the line fitting. In Section 4, we discuss interesting, individual sources. In Section 6, we generate the composite spectra for all 23 identified targets.

2 DATA COLLECTION

In this section, we present the target selection, spectroscopic observation using Keck and Gemini, and the data reduction.

2.1 Target selection

The selection of Type-2 QSO candidates in SDSS Stripe82 (B. Wang et al. 2025) is designed using the r-band photometry from SDSS/DESI Legacy Survey and $W4$ photometry from the All-sky Wide-field Infrared Survey Explorer (ALLWISE):

$$\begin{aligned} &12.62 < \mathrm{W4} < 14.62\,\mathrm{AB\ mag} \\ &\texttt{AND}\ \ \mathrm{SNR_{W4}} > 5 \\ &\texttt{AND}\ \ (r > 23\,\mathrm{AB\ mag}\ \ \texttt{OR}\ \ r - \mathrm{W4} > 8.38\,\mathrm{AB\ mag}) \end{aligned} \tag{1}$$

The SED of the hot dust torus peaks at rest-frame 10 μm. The WISE $W4$ bands probe the peak of the SED at $z \sim 2$. The upper magnitude limit of the $W4$ band is to select the most IR-luminous Type-2 QSOs. The lower limit of the magnitude range excludes bright stars or bright galaxies at low redshift. We further require candidates to be either non-detected in SDSS ($r > 23$ in the SDSS Stripe 82 catalogue) or with a red colour cut: $r - W4 > 8.38$ to exclude the Type-1 QSOs. This selection leads to 24 candidates in 164 deg^2 SDSS Stripe82 region.

2.2 Spectroscopic observation

2.2.1 Gemini/GNIRS spectra

To confirm the spectroscopic redshift of all 24 candidates, we use the GNIRS (J. H. Elias et al. 2006) on the Gemini North telescope to conduct the spectroscopic observation. These candidates are expected to be at $z \sim 2$ so the Hα and [O III] emission lines are expected to be covered by GNIRS. The candidates were observed under GN-2017B-Q-51 (PI: Gordon Richards) for several nights in 2017–09, 2017–10, and 2018–01. The grating was 32/mmSB which covers $0.9 - 2.4$ μm with spectral resolution of $R \sim 1100$. The exposure time for each candidate was 2400 s, and the observations were performed using an ABBA sequence. The spectroscopic classifications were published first in Y. Ishikawa et al. (2023) and B. Wang et al. (2025).

2.2.2 Keck/LRIS spectra

We choose 18 targets (17 Type-2 QSO candidates and one inconclusive target) to conduct a follow-up observation using the Keck Low Resolution Imaging Spectrometer (LRIS; J. B. Oke et al. 1995), to better confirm the redshifts and reveal the rest-UV spectra. The observations were taken on the night of 2022 September 27 and over the course of a 3-night run from 2022 October 26–28. We observed these targets using a 1.0 arcsec long-slit, 2×2 binning, 560 dichroic, and 600/4000 grating for the blue band with resolution ~ 4 Å covering 3040–5630 Å. The grating for the red band is: 400/8500, 1.0 arcsec long slit, resolution around 7 Å, $\Delta\lambda = 4762$ Å with the central wavelength 7980 Å. The average exposure time for each candidate is 1800 s. The Lyα and C IV emission lines are detected in the LRIS spectra. The typical seeing was 1.2 arcsec.

2.2.3 Keck/KCWI spectra

We further observed two targets with the Keck Cosmic Web Imager Integral Field Spectrograph (KCWI; P. Morrissey et al. 2018), to better constrain their redshift and reveal extended Lyα emission around these QSOs. We used Large Slicer, BL grating which covers 3258–5600 Å on the blue. The large slicer covers a sky area with $30'' \times 16''$. For the red side KCRM, we used RL grating covering 5550–9239 Å. The exposure time is 2×900 s and 4×430 s on the blue (KCWI) and red (Keck Cosmic Reionization Mapper, KCRM), respectively. The observation was conducted on the night of 2025 January 28. The typical seeing was 1.2 arcsec.

2.3 Data reduction

The Gemini and Keck observation data were reduced using the Pypeit pipeline (J. Prochaska et al. 2020). This pipeline can automatically produce calibrated 2D spectra. Then, we coadd the individual 2D spectra and use manual extraction to get the 1D spectra. The flux calibration and telluric correction are conducted using a standard star observed on the same night.

The Gemini/GNIRS observation contains two ABBA sequences, eight exposures for every target. The Pypeit pipeline produces four 2D spectra for each object. We check these 2D spectra to find the object manually and then coadd the 2D spectra using the object as a reference. This results in one coadded 2D spectrum. The 1D spectra are extracted manually or automatically from the coadded 2D spectra. Then, we apply the flux calibration and telluric correction on the 1D spectra using the standard star.

The Keck/LRIS observation contains two exposures in the blue and four exposures in the red for each object. Pypeit can produce 2D spectra for each individual exposure. Then, we coadd all the 2D spectra and then extract the 1D spectra from that.

The reduction for Keck/KCWI is more complex since this is an Integral Field Unit instrument. First, Pypeit can produce 2D spectra for each individual exposure. Then, we manually check the 2D spectra and find any emission line signal. After that, we combine all the 2D spectra to generate a data cube. The flux calibration is performed by extracting the spectrum of a standard star from the data cube. The wavelength of the emission line signal is used to generate the wavelength range of the white light. Finally, we manually extract the 1D spectra from the data cube based on the position of the target in the white light image.

Among our whole sample, 17 targets have GNIRS and LRIS spectra, two targets have GNIRS and KCWI spectra, and four targets only have GNIRS spectra. For the targets with multiwavelength spectra from Keck and Gemini, we first rebin and coadd these spectra. We rebin all spectra to a pixel scale of $\mathrm{d}v = 120\,\mathrm{km\,s^{-1}}$ in velocity space at the rest frame. For the overlapping region, we take the flux with higher signal-to-noise ratio (SNR) as the final flux.

Fig. 1 to Fig. 4 present example spectra in three separate wavelength windows for better visibility of key lines. Fig. 1 shows the two highest-z targets ($z > 3$). Fig. 2 shows the targets with narrow Hα emission. Figs 3 and 4 present some targets with broad Hα or Lyα emissions.

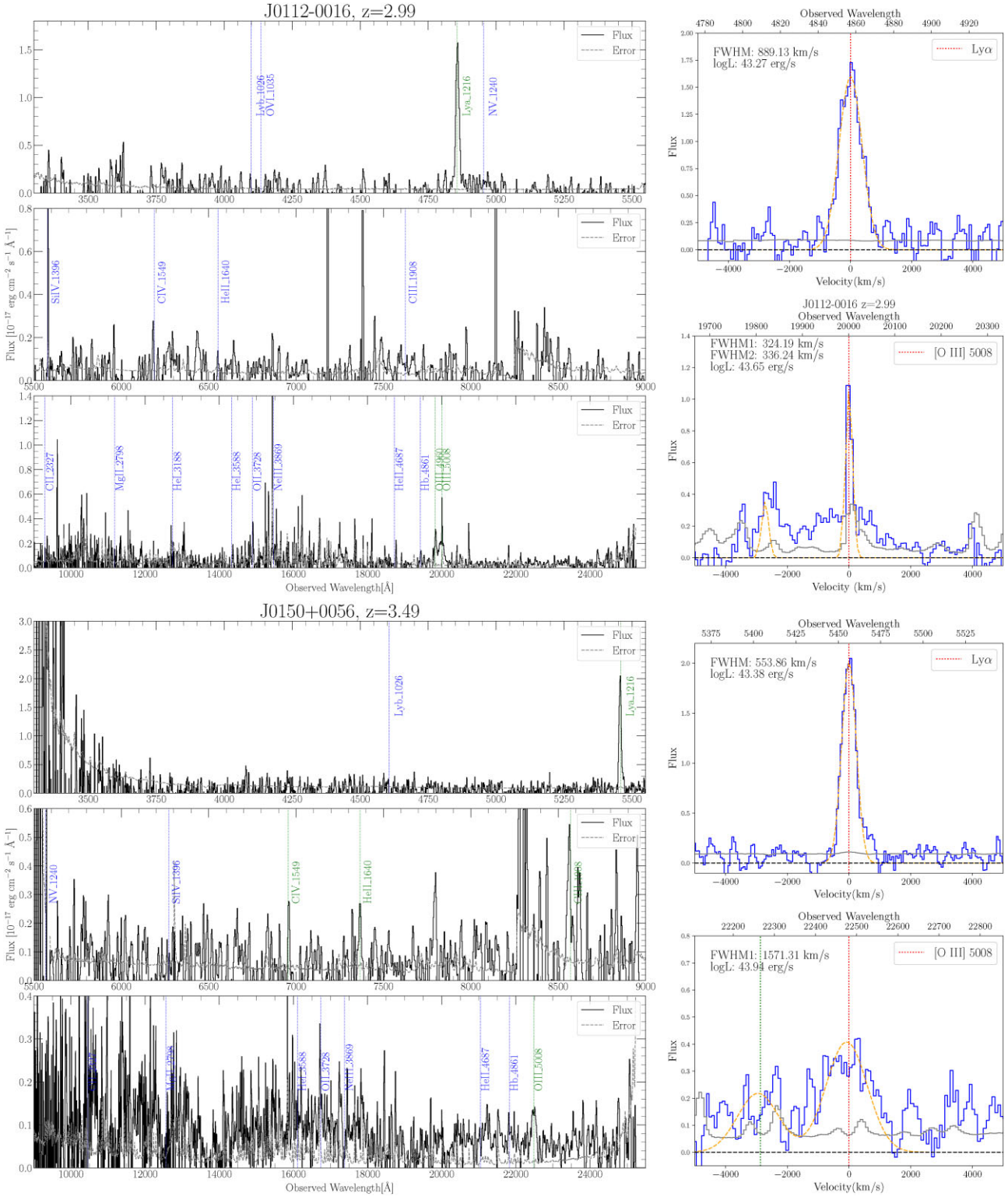

Figure 1. Example spectra from Keck and Gemini, and the fitted emission lines for 2 highest-z ($z > 3$) Type-2 QSO targets in our sample. The left panel shows the spectra from Keck/LRIS(or Keck/KCWI) and Gemini/GNIRS, the green lines mark the detected emission line, and the blue dashed lines are the undetected emission lines. The target name and redshift are shown in the title of the subplots. The right panel shows the Gaussian fitted emission lines for Ly α and [O III]. The flux is shown in blue, and the fitted Gaussian profile is shown in orange. The red lines mark the lince center of Ly α or [O III]λ5007, and the green line marks the line centre of [O III]λ4960. The FWHM and the line luminosity are labelled in the plots.

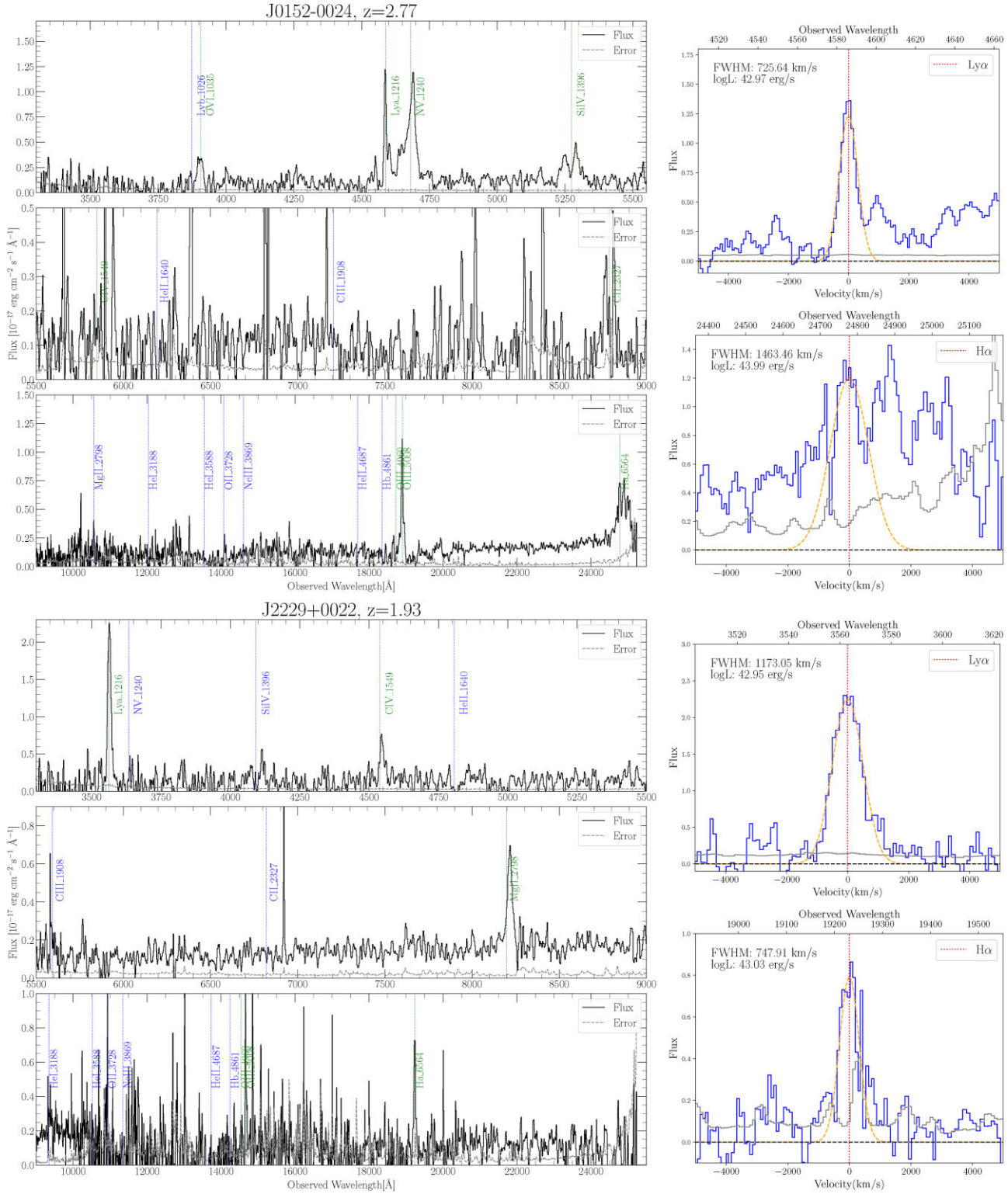

Figure 2. Example spectra and line fittings for two targets with narrow ($< 2000\,\mathrm{km\,s^{-1}}$) H α emission line. The top target has a strong absorption feature at the wavelength of Ly α and N v emission. The H α is located at the edge of the GNIRS coverage, making it difficult to measure the line width. The bottom panel shows a target with both narrow Ly α and narrow H α emission lines.

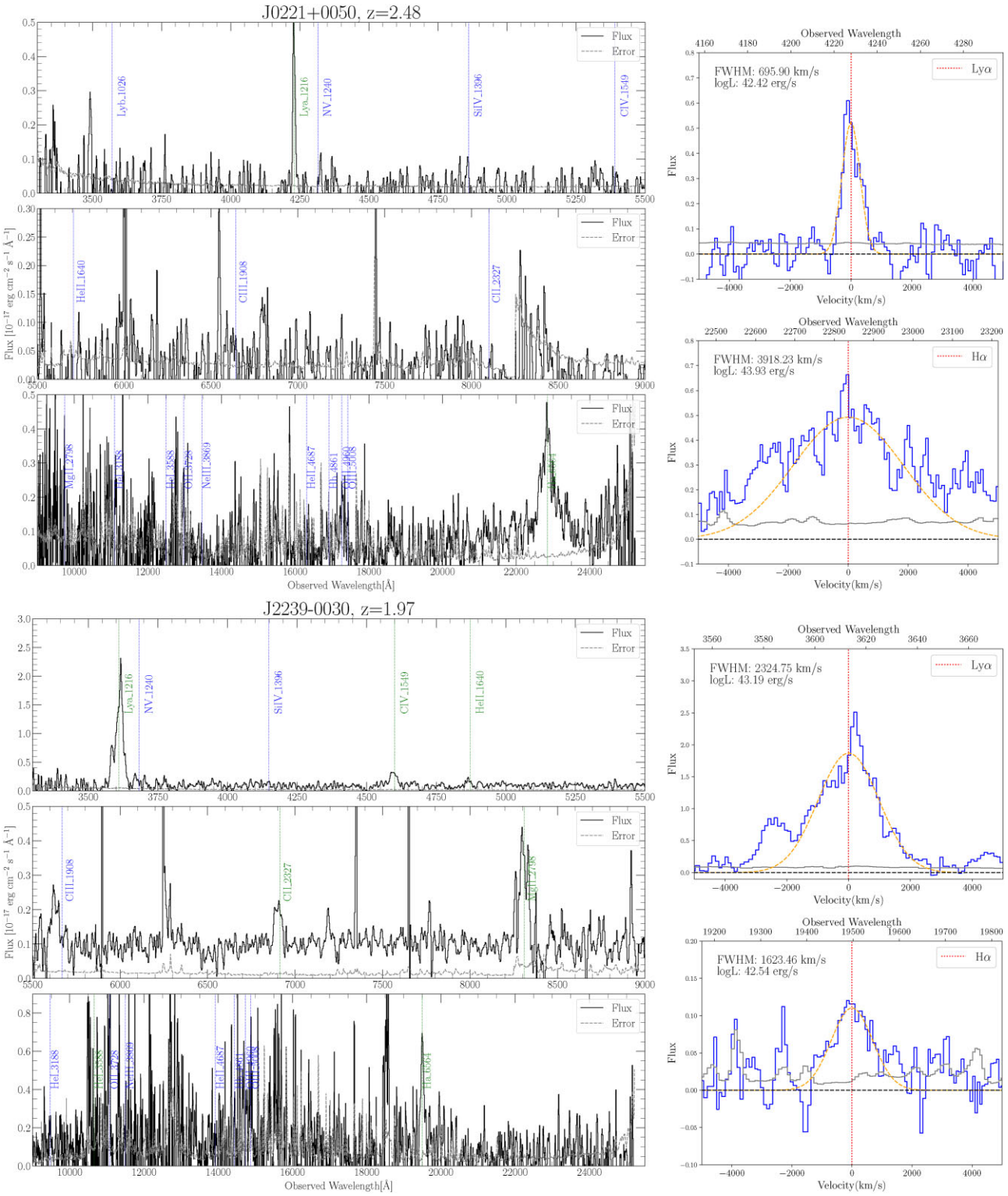

Figure 3. Example spectra and line fitting for two targets with broad H α or Ly α emissions. The upper panel shows a target J0221+0050 with broad H α and narrow Ly α emission. The broad emission lines are not expected for typical obscured QSOs, but it is a common feature in some ERQs and *JWST* AGNs. The lower panel shows a target with broad Ly α but narrow H α emission line.

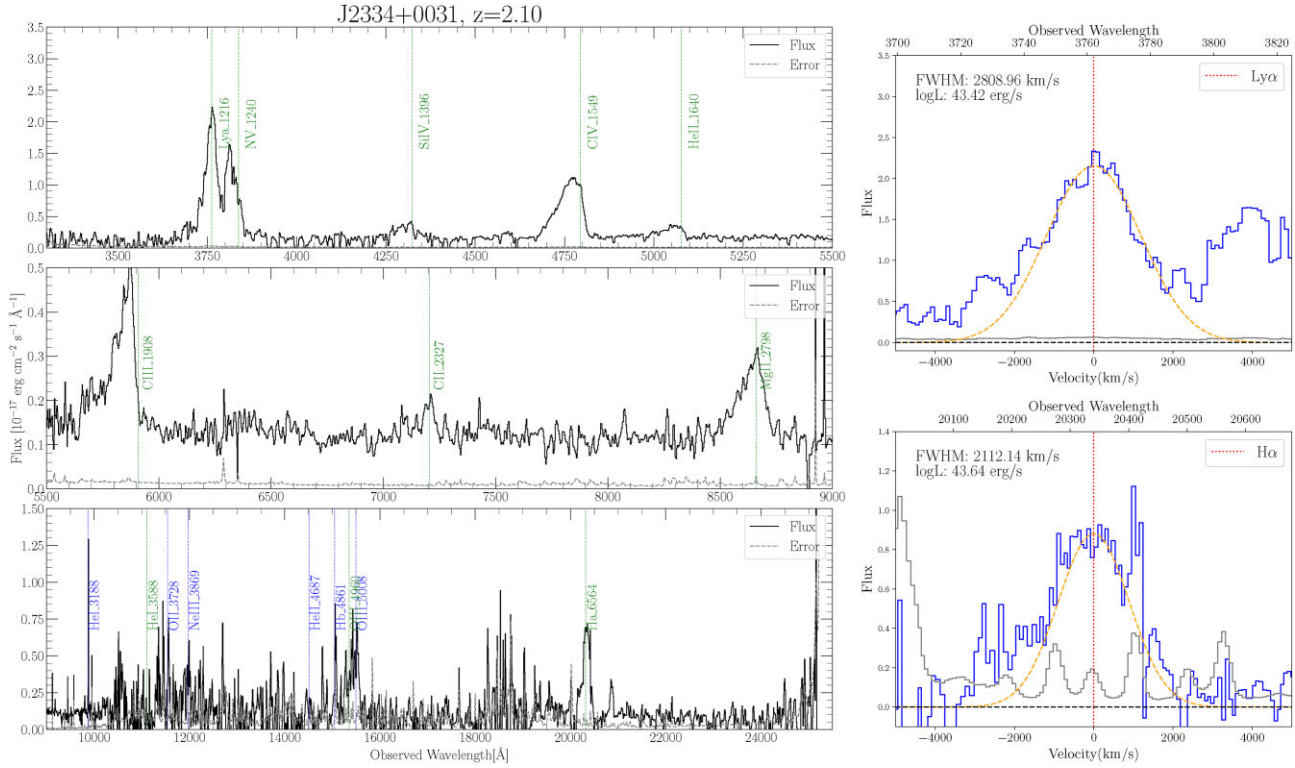

Figure 4. Example spectra and line fitting for one target with both broad Ly α and H α emission lines. This target J2334+0031 is the only target in our sample with both broad Ly α and H α emission lines. This target also has broad C IV, C III, and Mg II emission lines.

3 RESULTS

In this section, we present the emission line fitting results. We discuss the spectral diversity based on the line width of Ly α and H α, and the relation between the bolometric luminosity and the [O III] line luminosity.

3.1 Target identification

Among 24 targets, we see emission lines for 23 targets in the Gemini and Keck spectra. Based on the line detection, we identified 23 targets as real Type-2 or reddened Type-1 QSOs at $z \sim 2$, yielding a very high-success rate ($\sim$ 96 per cent). Of the 23 confirmed targets, 12 are at $z > 2$ ($\sim$ 52 per cent). One target, J0047+0003, remains inconclusive, since there are no obvious emission lines within the wavelength coverage of the Keck and Gemini spectra. It could be a very faint object or a spurious WISE source; identification of this target may require observations with *JWST*.

3.2 Line fitting

The redshift measurements are mainly based on the detection of Ly α and H α emission lines. For two targets, the H α emission is beyond the wavelength coverage of the Gemini/GNIRS, and we use Ly α and [O III] emission to measure the redshift.

First, we manually check the spectra and identify the emission lines to determine the rough spectroscopic redshift. Then, we fit a Gaussian profile to every emission line to get the accurate redshift, line width, and line luminosity. For single emission lines like Ly α and H α we fit a single Gaussian profile. For other lines like [O III], two Gaussian profiles are used to fit the doublet.

The fitted line profiles are shown in the right subplots from Fig. 1 to Fig. 4. The observed flux is shown in blue, and the fitted Gaussian profiles are shown in orange. The red line marks the fitted line centre. The full width at half-maximum (FWHM) and the line luminosity are labelled on the upper left of each plot.

3.3 Ly α and H α emission lines

Among the 23 identified targets, 13 targets have Ly α detection in the Keck spectra, and 21 targets have H α detection in the Gemini spectra. The fitted line properties of Ly α and H α are summarized in Table 1.

For the 11 targets with both Ly α and H α detected, we can compare the line properties of these two lines. We define a broad line as FWHM $> 2000\,\mathrm{km\,s^{-1}}$ and a narrow line as FWHM $< 2000\,\mathrm{km\,s^{-1}}$ (N. L. Zakamska et al. 2003; L. Hao et al. 2005). According to this definition, six targets have narrow Hα and narrow Ly α emission lines, three targets have broad H α and narrow Ly α emission lines, one target has narrow H α and broad Ly α emission lines, and one target has broad H α and broad Ly α emission lines. The targets in our sample show a diversity of this line width. The relation of Ly α and H α FWHM is shown in Fig. 5.

3.3.1 Narrow H α and narrow Ly α

A narrow emission line ($< 2000\,\mathrm{km\,s^{-1}}$) is the typical identifying spectral feature for Type-2 QSOs at low-z (e.g. N. L. Zakamska et al. 2003; R. Alexandroff et al. 2013; M. Lacy et al. 2013). We have five targets with both the Ly α and H α detections that are narrow, which is consistent with these previous Type-2 QSOs found at low redshift.

Table 1. The redshift, emission lines used to get the redshift, line luminosity, and FWHM of Ly α and H α for all the targets in this sample.

Target	z	Ref line	$\log(L_{Ly\alpha}(\mathrm{erg\,s^{-1}}))$	$\mathrm{FWHM}_{Ly\alpha}(\mathrm{km\,s^{-1}})$	$\log(L_{H\alpha}(\mathrm{erg\,s^{-1}}))$	$\mathrm{FWHM}_{H\alpha}(\mathrm{km\,s^{-1}})$	Spectra
J0024−0012	1.53	[O III], H α	–	–	$10^{42.92}$	2144.99	GNIRS+LRIS
J0041−0029	2.09	H α	–	–	42.92	438.86	GNIRS+LRIS
J0047+0003	–	–	–	–	–	–	GNIRS+LRIS
J0054+0047	2.17	H α	–	–	42.76	879.38	GNIRS+LRIS
J0105−0023	1.87	Ly α,H α	42.72	1448.37	42.81	699.84	GNIRS+LRIS
J0112−0016	2.99	Ly α,[O III]	43.27	889.15	–	–	GNIRS+LRIS+KCWI
J0113+0029	2.33	H α	–	–	43.08	1107.72	GNIRS
J0130+0009	2.51	H α	–	–	43.82	3272.59	GNIRS
J0149+0052	1.85	H α	–	–	43.10	924.22	GNIRS
J0150+0056	3.49	Ly α,[O III]	43.38	553.86	–	–	GNIRS+KCWI
J0152−0024	2.78	Ly α,H α	42.97	725.51	43.96	1382.12	GNIRS+LRIS
J0213+0024	1.81	H α	–	–	43.74	3849.89	GNIRS+KCWI
J0214−0000	1.63	H α	–	–	43.21	1145.28	GNIRS+LRIS
J0215+0042	0.88	H α	–	–	43.17	2683.46	GNIRS
J0221+0050	2.48	Ly α,H α	42.43	695.90	43.91	3918.23	GNIRS+LRIS
J2229+0022	1.93	Ly α,H α	42.95	1173.02	43.03	747.91	GNIRS+LRIS
J2233−0004	1.60	H α	–	–	43.21	1237.80	GNIRS+LRIS
J2239−0030	1.97	Ly α,H α	43.19	2324.75	42.52	1511.77	GNIRS+LRIS
J2239−0054	2.09	Ly α,H α	43.54	1734.92	42.78	1295.67	GNIRS+LRIS
J2243+0017	1.91	Ly α,H α	42.72	1295.17	43.57	4776.12	GNIRS+LRIS
J2258−0022	2.42	Ly α,H α	42.65	1508.45	43.07	764.07	GNIRS+LRIS
J2259−0009	1.89	Ly α,H α	42.39	907.63	43.68	3009.32	GNIRS+LRIS
J2329+0020	2.67	Ly α,H α	42.65	1007.21	44.15	2850.25	GNIRS+LRIS
J2334+0031	2.10	Ly α,H α	43.42	2808.96	43.64	2112.14	GNIRS+LRIS

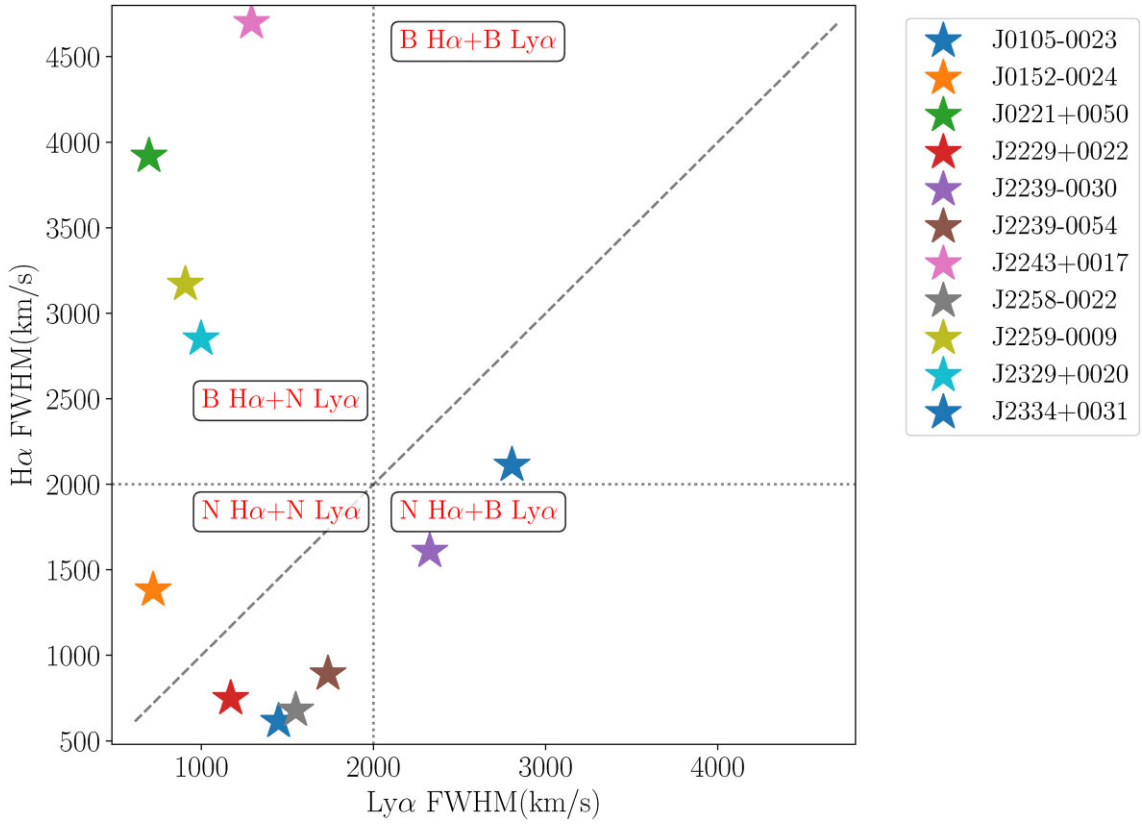

Figure 5. The FWHM of H α and Ly α of 11 targets in our sample. The X-axis is the FWHM of the Ly α emission lines, and the y-axis is the H α FWHM. The 2000 km s^{-1} is marked as black dashed lines. According to this definition, five targets have narrow H α and narrow Ly α emission lines, four targets have broad H α and narrow Ly α emission lines, one target has narrow H α and broad Ly α emission lines, and one target has broad H α and broad Ly α emission lines. Our targets show spectral diversity in the line width.

3.3.2 *Broad H α and broad Ly α*

Presence of broad emission lines defines Type-1 QSOs. One target, J2334+0031, has broad lines in both the Ly α and H α detections (see Fig. 4). This target also has broad C IV, C III, and Mg II emission lines. The SED and photometry of this target are obviously different from Type-1 QSOs, as it is redder than the extreme red QSOs in SDSS (B. Wang et al. 2025).

3.3.3 *Broad H α and narrow Ly α*

Four of our targets have broad H α emission lines but narrow Ly α emission lines. A broad H α emission line is usually not expected given the standard picture of Type-2 QSOs based on low-z ($z \lesssim 1$) observations, but it is detected in many *JWST* AGNs (or LRDs) (e.g. Y. Harikane et al. 2023; V. Kokorev et al. 2023). In our sample, 7/21 targets have broad H α emission lines. It is puzzling that we still see the broad H α emission lines despite using red colours to select the most obscured QSOs. One possible scenario is that there is obscuration toward the H α emitting region, then the UV-emitting region would be fully obscured and Ly α would be produced on larger scales by a different mechanism and be narrower, or at least have different kinematics as they represent different regions. In our SED fitting paper (B. Wang et al. 2025), we show that the rest-UV/optical composite SEDs of our targets are very red and similar to LRDs. These broad-line targets may further reveal the potential connection of our Type-2 QSOs to *JWST* LRDs with broad emission lines.

3.3.4 *Narrow H α and broad Ly α*

We have one target with narrow H α but broad Ly α emission lines. The mechanism to produce the inconsistency of these two lines is still unclear. One possible scenario is that the broad Ly α is emitted in the broad-line region (BLR) while the narrow H α arises from the narrow line region (H. Zhou et al. 2006). It could also be due to so-called selective extinction, whereby internal reddening may suppress broad Balmer emission more than Ly α emission (H. Netzer, B. J. Wills & D. Wills 1982).

4 DISCUSSION OF INDIVIDUAL TARGETS

In this section, we discuss some special targets with interesting spectral features.

4.1 J0150+0056

This target is the highest redshift ($z = 3.49$) Type-2 QSO in our sample (lower panel in Fig. 1). Initially, this target only had a Gemini/GNIRS spectrum, and we considered the single emission line to be H α (Y. Ishikawa et al. 2023).

However, after the Keck/KCWI observations, we identified a strong Ly α emission line in KCWI, and the emission line in GNIRS spectra turns out to be [O III]. The redshift of this target is $z = 3.49$ by fitting the line centre of Ly α and [O III]. This target is also the brightest target in our sample ($L_{\rm bol} = 10^{48.08}$ erg s^{-1}, see B. Wang et al. (2025) for the $L_{\rm bol}$ estimate). Assuming the Eddington limit,

the black hole mass should be above $10^{9.98}\,M_{\odot}$, placing it at the bright and massive end of SMBHs at this redshift.

4.2 J0152−0024

This target is a $z = 2.77$ Type-2 QSOs confirmed by the Keck/LRIS and Gemini/GNIRS spectra (upper panel in Fig. 2). The Hα line of this target is located at the edge of the GNIRS coverage, so it is difficult to measure the full line FWHM.

There is a strong absorption line feature at Lyα and the N vλ1240 emission line. We measure the Lyα emission line has FWHM about 720.62 km s^{-1}, but this is underestimated, due to the strong absorption feature. We also notice that a similar absorption feature is seen at the Si IVλ1396 emission line. This target also has an O VIλ1035 line detection.

4.3 J0221+0050

J0221+0050 object is a $z = 2.48$ Type-2 QSO confirmed by both the Keck and Gemini spectra (upper panel in Fig. 3). Only Hα and Lyα emission lines are detected in the spectra. The Hα has a broad ~ 3918 km s^{-1}

component, but the Lyα is narrow (~ 695 km s^{-1}). Such a broad Hα emission line is not expected in typical Type-2 QSOs, but is commonly detected in many *JWST* LRDs. Considering the similar UV SED shape of these targets and the *JWST* LRDs (B. Wang et al. 2025), such broad-line obscured QSOs could be the lower-z analogues of *JWST* LRDs.

4.4 J2334+0031

Target J2334+0031 is the only object with both broad Hα and Lyα in our sample (see Fig. 4). This target is confirmed to be a Type-2 QSO at $z = 2.09$ by Gemini and then further observed by Keck/LRIS. The FWHM of Lyα for this target is 2808 km s^{-1} and the Hα is 2112 km s^{-1}. Such a line width is similar to the typical Type-1 QSOs. However, the photometry and SED of this target are different from the typical UV-bright Type-1 QSO (see fig. B1 in B. Wang et al. 2025).

Besides, there is a blueshift of the N v emission line. Due to the low resolution of Keck/LRIS, we do not know if there is strong absorption between the Lyα and N v emission line. We are also not sure if this causes the blueshift of the N v emission line. The C IV, C III, and Mg II emission line show an asymmetric line profile, and the line peak of C III shows a ~ 1776 kms^{-1} offset from the expected position. The broad and asymmetric line profiles are reported in some ERQs (Perrotta et al. 2019; M. Villar Martín et al. 2020; J. Gillette et al. 2024). The broad-line regions in ERQs are typically outflow-dominated, and these outflows can produce strong blueshifted or broad emission lines (e.g. J. Gillette et al. 2024). ERQs could also be very luminous Type-1 quasars viewed at an intermediate orientation, and this orientation allows a direct view of the outer part of the large broad-line region (e.g. M. Villar Martín et al. 2020). These two scenarios can explain the broad and asymmetric line profiles for this target J2334+0031.

5 THE $L_{[OIII]} - L_{bol}$ SCALING RELATION

The [O III] line is forbidden and is expected to arise from the narrow-line region, because its critical density, $n_{crit} \simeq 7 \times 10^5$ cm^{-3} is exceeded by the much higher density gas, $n_{H|} \sim 10^{9-11}$ cm^{-3} broad-line region (D. E. Osterbrock & G. J. Ferland 2006). In both Type-1 and Type-2 QSOs, [O III] is powered by the same UV emission from the AGN (J. Stern & A. Laor 2012). However, the UV continuum is obscured and reprocessed by the mid-IR emission in Type-2 QSOs. Thus, a relation between the [O III] line luminosity and the mid-IR luminosity (or bolometric luminosity determined from the mid-IR emission) is expected (e.g. N. L. Zakamska et al. 2003; A. Lamastra et al. 2009; M. Lacy et al. 2013).

M. Lacy et al. (2013) studied this relation with a sample of ~ 100 Type-2 QSOs at $z < 2$. Specifically, they observed that the luminosity of the [O III]λ5007 line, without any extinction correction, strongly correlates with the mid-IR luminosity, νL_{ν}, at 15 μm. We use the torus template from M. Stalevski et al. (2016) and our composite SED in B. Wang et al. (2025) to determine the relation between the luminosity at 15 μm (observed frame at $z \sim 2$) and the bolometric luminosity:[1]

$$L_{bol} = 6.03 \times L_{15\mu m}. \quad (2)$$

Using this relation, the luminosity at 15 μm in M. Lacy et al. (2013) can be used to compute the bolometric luminosity, which assumes their targets have the same mid-IR SED shape as our targets. The results are shown as the green dots in Fig. 6. A green dotted line shows a simple power-law fit (linear fit in the log) to these data.

In our Type-2 sample, 13/23 targets have an [O III] detection. We use a double-Gaussian profile with wavelength separation and relative line strength set by atomic physics to fit the emission line. The FWHM and the luminosity of this double-line can be estimated from the fitting. The [O III] luminosity is here defined to be the luminosity of [O III]λ5007 alone. The fitted parameters are shown in Table 2, and the relation between the [O III] luminosity and the bolometric luminosity for our targets is shown as the coloured stars in Fig. 6. Since our targets do not have Hβ line detection, we could not conduct the extinction correction using.

We also show the $L_{[OIII]} - L_{bol}$ relation from A. Lamastra et al. (2009), N. L. Zakamska et al. (2016), and S. M. LaMassa et al. (2010). A. Lamastra et al. (2009) estimate the bolometric correction $C_{[OIII]} = L_{bol}/L^{c}_{[OIII]}$ in different [O III] luminosity ranges. The bolometric luminosity is estimated from the X-ray luminosity. The $L^{c}_{[OIII]}$ here is the extinction corrected [O III] luminosity using:

$$L^{c}_{[O\,III]} = L_{[O\,III]} \left(\frac{(H\alpha/H\beta)_{obs}}{3.0} \right)^{2.94} \quad (3)$$

They found a mean value of $C_{[OIII]}$ in the luminosity ranges log $L_{[OIII]}$ = 38–40, 40–42, and 42–44 of 87, 142, and 454, respectively. However, we still plot this relation in Fig. 6 as for comparison.

N. L. Zakamska et al. (2016) and S. M. LaMassa et al. (2010) summarized the relation between the luminosity at 13.5 μm and the [O III] luminosity for Type-2 QSOs to be: logνL_{ν}[13.5μm] = 12.1 + 0.77log$L$[OIII] and logνL_{ν}[13.5μm] = 15.7 + 0.68log$L$[OIII]. We assume their targets have a similar SED shape to ours, then we

[1]We have a composite SED for Type-2 QSOs in B. Wang et al. (2025). From that composite SED, we can get the luminosity at 15 μm. The composite SED contains a torus model using the template from M. Stalevski et al. (2016), and then we calculate the torus luminosity by integrating the torus model. The bolometric luminosity is estimated using equation (4) in B. Wang et al. (2025) assuming $R = 0.5$. After that, we apply the relation between the 15 μm luminosity and bolometric luminosity.

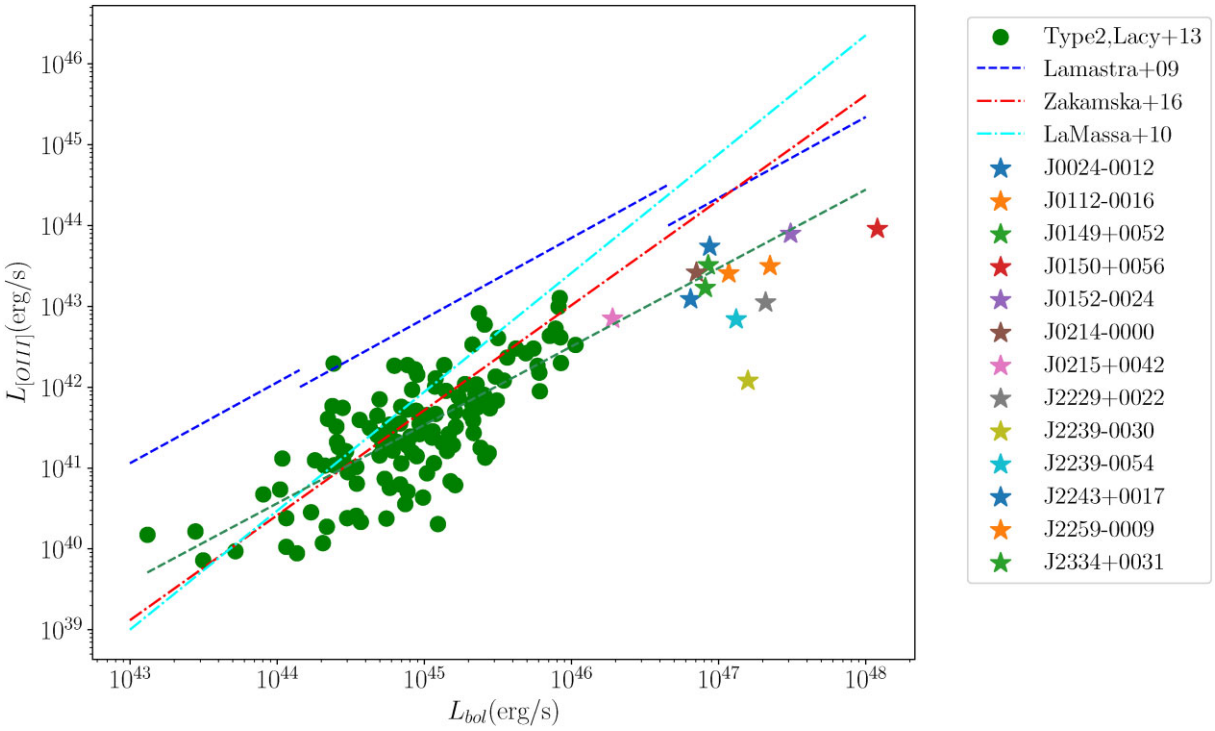

Figure 6. The relation between the luminosity of the [O III] emission line and the bolometric luminosity. The relations from A. Lamastra et al. (2009), S. M. LaMassa et al. (2010), and N. L. Zakamska et al. (2016) are shown as blue, cyan, and red lines. The green dots are the Type-2 AGN measurements from M. Lacy et al. (2013). The luminosities at 15 μm of these targets are scaled to estimate the bolometric luminosity. The coloured stars are the measurements of 13 targets with [O III] detection in our sample. The green dashed line presents a power-law fit (linear fit on log scale) to the green data points. The [O III] luminosities in relations from A. Lamastra et al. (2009), S. M. LaMassa et al. (2010), and N. L. Zakamska et al. (2016) are all extinction corrected. The $L_{[OIII]}$ in M. Lacy et al. (2013) and our sample is not dust extinction corrected due to the non-detection of H β or H α emissions. Compared to the three corrected relations, our targets show a lower [O III] luminosity because of the dust extinction. However, even compared to the uncorrected sample in M. Lacy et al. (2013), the [O III] luminosity is still below the fitting (green dotted line). Our targets are about 100× brighter than the low-z objects in M. Lacy et al. (2013), but the [O III] luminosity does not increase accordingly.

Table 2. The red shift, [O III] line property, and bolometric luminosity for 13 targets.

Target	z	$\log(L_{[OIII]}(\mathrm{erg\,s^{-1}}))$	$\mathrm{FWHM}_{4960}(\mathrm{km\,s^{-1}})$	$\mathrm{FWHM}_{5007}(\mathrm{km\,s^{-1}})$	$\log(L_{\mathrm{bol}})$
J0024−0012	1.53	43.04	–	1045.61	46.81
J0112−0016	2.99	43.55	336.24	324.74	47.35
J0149+0052	1.85	43.57	1289.20	1417.45	46.93
J0150+0056	3.49	43.91	–	2712.18	48.08
J0152−0024	2.78	43.93	–	1047.80	47.49
J0214−0000	1.63	43.43	616.39	450.66	46.85
J0215+0042	0.88	42.81	–	1125.59	46.28
J2229+0022	1.93	43.03	–	690.97	47.32
J2239−0030	1.97	42.08	–	369.25	47.20
J2239−0054	2.09	42.79	–	924.68	47.12
J2243+0017	1.91	43.74	1216.76	1022.27	46.94
J2259−0009	1.89	43.29	–	1711.87	47.07
J2334+0031	2.10	43.23	572.67	653.70	46.91

can use our SED to adopt the relation between the $L_{13.5\mu m}$ and the L_{bol}:

$$L_{\mathrm{bol}} = 6.01 \times L_{13.5\mu m} \quad (4)$$

We plot the adopted bolometric luminosity and [O III] line luminosity as red and cyan dotted lines in Fig. 6.

The [O III] luminosities in relations from A. Lamastra et al. (2009), S. M. LaMassa et al. (2010), and N. L. Zakamska et al. (2016) are all extinction corrected. The $L_{[OIII]}$ in M. Lacy et al. (2013) and our sample is not dust extinction corrected due to the fact that we do not always detect both the H β or H α lines. Compared to the three extinction corrected relations, our targets show a lower [O III] luminosity, which is likely due to extinction. However, even comparing to the uncorrected sample in M. Lacy et al. (2013), the [O III] luminosity is still below our fit to their data (green dotted line). Our targets are about 100× brighter than the low-z objects in M. Lacy et al. (2013), but the [O III] luminosity does not increase accordingly.

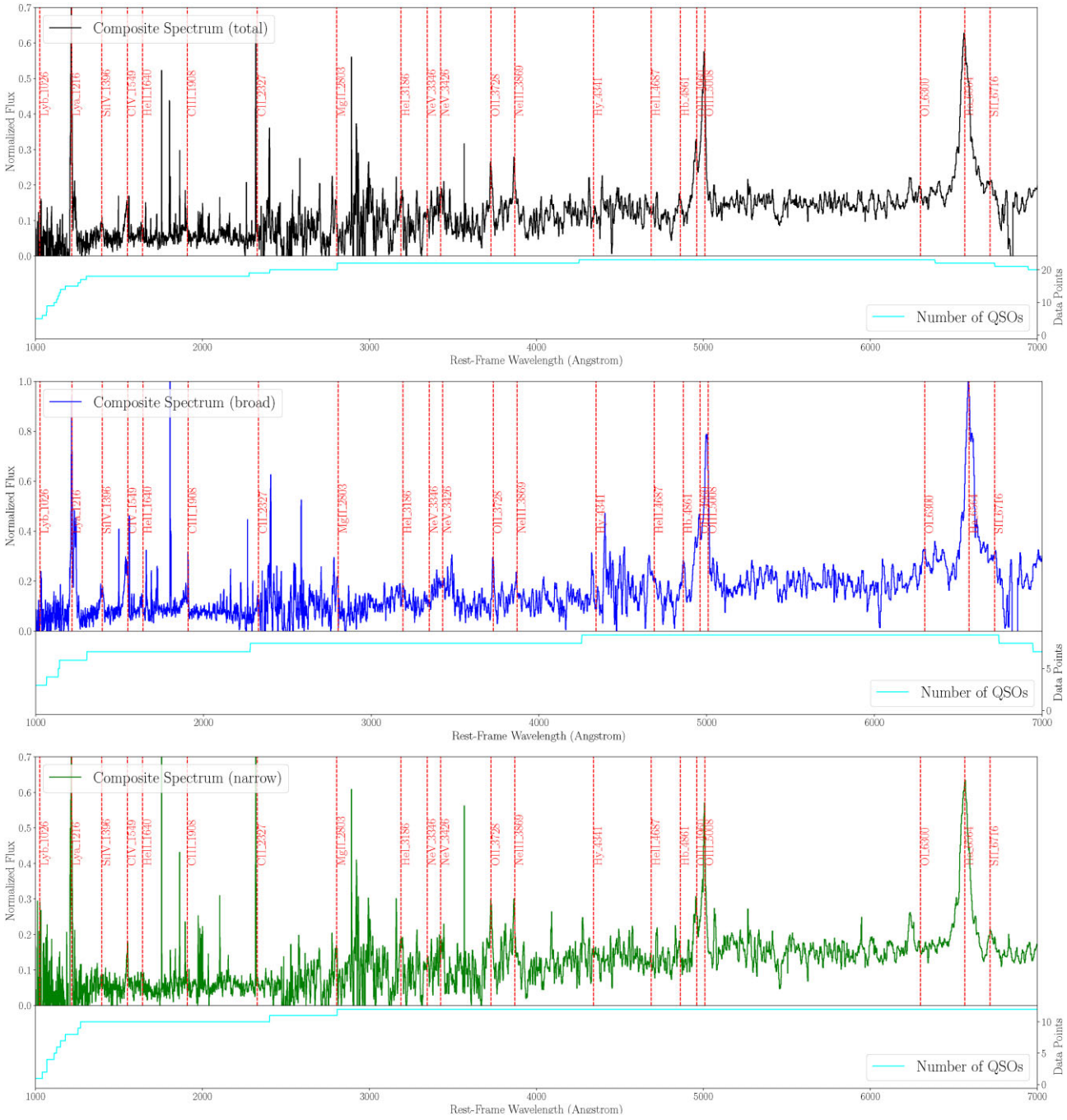

Figure 7. The composite spectra for 23 targets in our sample. The top panel shows the composite spectra for all 23 targets, and the median panel shows the composite spectra for nine targets with broad Hα emissions. The bottom panel shows the composite spectrum only for 12 targets with narrow Hα emission lines. The red dashed lines mark the typical emission lines for QSOs. The bottom subplot shows the number of QSOs contributing to each wavelength.

6 COMPOSITE SPECTRA

In this section, we generate composite spectra for all 23 identified targets to better understand the spectral properties of Type-2 QSOs. To generate the composite spectra, we first define the scaling parameter using the WISE W4 flux for each target. All 23 targets are scaled to the median value of the WISE W4 flux (6.53 mJy), and then the same scaling parameter is applied to the spectra. Then we take the median flux value at each wavelength to get the composite spectra. The final composite spectra is shown in Fig. 7. The top panel shows the composite spectra for all 23 targets (black), and the middle panel shows the composite spectra for nine targets with broad Hα emission (blue). Here we further include target J0152−0024 into the broad Hα group. Since the Hα emission for this target fall at the edge of the wavelength coverage, making the fitted FWHM with a single Gaussian profile could be an underestimate of the intrinsic value. The bottom panel shows the composite spectrum only for 12 targets with narrow Hα emission lines (green). The red dashed lines mark the typical emission lines for QSOs. The bottom subplots show the number of QSOs contributing to each wavelength.

From our composite spectra, we see the tentative detection of some relative weak rest-optical lines like: [O II]λ3782, [Ne III]λ3869, H β, [O I]λ6300, and [S II]λ6716. The Type-2 composite spectra in M. Lacy et al. (2004) show both strong high-ionization narrow lines and low-ionization lines such as [O I], but it lacks coronal lines. K. N. Hainline et al. (2011) generated the rest-UV composite spectra for Type-2 AGNs and find a median velocity difference between Ly α and He II to be $\Delta v = 208\,\mathrm{km\,s^{-1}}$. They also find a red UV continuum slope produced by dust extinction and some rare emission lines like N IV]λ1486. Compare to these two composite spectra from previous surveys, our composite spectra do not show a strong detection of He II emission line. Our composite cover the rest-optical emissions which K. N. Hainline et al. (2011) does not cover, and a comparison between our composite and the composite in M. Lacy et al. (2013) could give us an idea if the obscured population is evolving with redshift. A detailed discussion between different Type-2 composite spectra will be presented in a future paper.

The weak lines ([O II]λ3782, [Ne III]λ3869, Hβ, [O I]λ6300, and [S II]λ6716) are usually used to build the "Baldwin, Phillips & Terlevich" (BPT) line ratio diagram to identify AGNs or galaxies (e.g. G. Mazzolari et al. 2025). However, even the most powerful ground-based telescopes like Keck and Gemini cannot detect these weak lines individually for the most luminous Type-2 QSOs at $z \sim 2$. Only *JWST* observations can further reveal these weak lines and help us better understand the relation between these obscured populations and other galaxies or AGNs.

7 CONCLUSION

In this paper, we present the spectroscopic observation results for 23 IR-luminous Type-2 QSOs using Keck and Gemini. These targets are selected using an r − W4 colour cut, and the Gemini and Keck spectroscopic observations confirm that these targets are at $z = 0.88 - 3.49$ (12 are at $z > 2$). The SED fitting results are published in a previous paper (B. Wang et al. 2025). Our main conclusions based on these spectra are:

(i) Our targets show significant spectral diversity in the relative widths of their emission lines. Five of our targets have narrow Ly α and H α emission lines, which is consistent with some typical Type-2 QSOs. One of our targets J2334+0041 has both broad Ly α and H α emission, which is more similar to typical Type-1 QSOs. However, the UV-faintness and the SED shape make it different from the UV-bright Type-1 QSOs; we consider this target to be like some ERQs. Four of our targets have broad H α and narrow Ly α emission. This feature is commonly seen in some *JWST* LRDs or broad-line AGNs. One of our targets has narrow H α and broad Ly α emission, which could be caused by the viewing angle or the lines are raised from different regions (the broad Ly α is emitted in the BLR while the narrow H α arises from the narrow line region).

(ii) Three out of our targets have broad H α and narrow Ly α emission. Such a broad line is not usually seen in the low-z Type-2 QSOs, but it is a common feature for some *JWST* broad-line AGNs. Considering the similar UV SED shape (see B. Wang et al. 2025), these targets could be the analogue of *JWST* LRDs at lower-z. Our selection can uncover the diverse obscured population and could bridge the gap between low-z obscured QSOs and the *JWST* AGNs.

(iii) Compared to the previous Type-2 QSO samples at lower-z ($z < 2$) in M. Lacy et al. (2013), our targets have bolometric luminosity over a hundred times larger. Since most of our targets do not have H β detections, it is not possible to perform extinction corrections of the [O III] line luminosity via the the Balmer decrement. Compared to the uncorrected [O III] luminosity and bolometric luminosity relation in M. Lacy et al. (2013), our targets show relatively lower [O III] luminosity. The physics behind this low [O III] luminosity is not yet clear.

(iv) We constructed composite spectra for all 23 targets, only broad H α targets, and only narrow H α targets. The composite spectra allow us to detect many weak lines, which is useful for us to better understand the spectral properties of this obscured population. However, the detection of such weak lines for individual objects, key for understanding the spectral diversity, would require higher signal-to-noise ratio observations with *JWST*.

Prior to the launch of *JWST*, multiwavelength surveys have build a large sample of obscured QSOs at $z < 2$. The recent *JWST* observations suggest the presence of a large obscured population at $4 < z < 9$. Our Type-2 QSO survey can bridge the gap between these two obscured populations at cosmic noon ($2 < z < 4$) and uncover the diverse obscured population. Building a census of Type-2 QSOs across cosmic time is key to understanding two questions: (1) If the obscured population is evolving; (2) what is the true nature of obscured QSOs. Gemini and Keck are the most powerful spectroscopic telescopes on the ground. They are sufficiently sensitive to detect the strongest emission lines and measure the redshifts of these heavily obscured QSOs with exposure times of 0.5–1 h. Gemini spectra cover the rest-frame optical that is usually covered by low-z surveys, but our S/N is quite poor. So it is hard to make a comparison and reveal any differences. At low-z one does not have the rest-UV spectra that we cover in this paper, making the low-z to high-z comparison challenging. We see significant spectral diversity in the relative widths of the emission lines. Some targets show very broad emissions despite the obscuration. They do not seem to follow from a simple unification explanation. The higher S/N *JWST* spectra may allow us to do a comparison across the cosmic time to study if the obscured population is evolving. Besides, the detection of the weak emission lines will allow us to build a new BPT diagram, to better understand the relation of the obscured populations and other galaxies and AGNs.

ACKNOWLEDGEMENTS

BW and ZC were supported by the National Key R&D Program of China (grant no. 2023YFA1605600), the National Science Foundation of China (grant no. 12073014), the science research grants from the China Manned Space Project with No. CMS-CSST-2021-A05, and Tsinghua University Initiative Scientific Research Program (No. 20223080023).

J-TS was supported by the Deutsche Forschungsgemeinschaft (DFG, German Research Foundation) – Project number 518006966.

DATA AVAILABILITY

The Gemini/GNIRS spectra are public in the Gemini Observatory Archive under the proposal ID GN-2017B-Q-51. The Keck spectra are all public on the Keck Data Archival (KOA). The reduced version of all the spectra can be found at https://github.com/samwang141224/Type-2QSOs/tree/main/spec-data.

REFERENCES

Akins H. B. et al., 2025, ApJ, 991, 37
Alexandroff R. et al., 2013, MNRAS, 435, 3306
Alexandroff R. M. et al., 2018, MNRAS, 479, 4936

Alonso-Herrero A. et al., 2006, ApJ, 640, 167
Andonie C. et al., 2025, MNRAS, 539, 2202
Antonucci R., 1993, ARA&A, 31, 473
Assef R. J. et al., 2013, ApJ, 772, 26
Assef R. J. et al., 2015, ApJ, 804, 27
Bañados E. et al., 2018, Nature, 553, 473
Banerji M., Alaghband-Zadeh S., Hewett P. C., McMahon R. G., 2015, MNRAS, 447, 3368
Brand K. et al., 2007, ApJ, 663, 204
Brandt W. N., Alexander D. M., 2015, A&AR, 23, 1
Cai Z. et al., 2017, ApJ, 837, 71
Chaussidon E. et al., 2023, ApJ, 944, 107
DESI Collaboration, 2024, AJ, 168, 58
Dey A. et al., 2008, ApJ, 677, 943
Donley J. L. et al., 2012, ApJ, 748, 142
Eisenhardt P. R. M. et al., 2012, ApJ, 755 , 173
Elias J. H., Joyce R. R., Liang M., Muller G. P., Hileman E. A., George J. R., 2006, in McLean I. S., Iye M., eds, Proc. SPIE Conf. Ser. Vol. 6269, Ground-based and Airborne Instrumentation for Astronomy. SPIE, Bellingham, p. 62694C
Gillette J., Hamann F., Lau M. W., Perrotta S., 2024, MNRAS, 527, 950
Glikman E. et al., 2018, ApJ, 861, 37
Greene J. E. et al., 2024, ApJ, 964, 39
Haas M. et al., 2004, A&A, 419, L49
Hainline K. N., Shapley A. E., Greene J. E., Steidel C. C., 2011, ApJ, 733, 31
Hamann F. et al., 2017, MNRAS, 464, 3431
Hao L. et al., 2005, AJ, 129, 1795
Harikane Y. et al., 2023, ApJ, 959, 39
Hopkins P. F., Hernquist L., Cox T. J., Di Matteo T., Robertson B., Springel V., 2006, ApJS, 163, 1
Inayoshi K., 2025, ApJ, 988, L22
Ishikawa Y., Wang B., Zakamska N. L., Richards G. T., Hennawi J. F., Rivera A. B., 2023, MNRAS, 522, 350
Kocevski D. D. et al., 2023, ApJ, 954, L4
Kokorev V. et al., 2023, ApJ, 957, L7
LaMassa S. M., Heckman T. M., Ptak A., Martins L., Wild V., Sonnentrucker P., 2010, ApJ, 720, 786
Lacy M. et al., 2004, ApJS, 154, 166
Lacy M. et al., 2013, ApJS, 208, 24
Lacy M., Ridgway S. E., Sajina A., Petric A. O., Gates E. L., Urrutia T., Storrie-Lombardi L. J., 2015, ApJ, 802, 102
Lamastra A., Bianchi S., Matt G., Perola G. C., Barcons X., Carrera F. J., 2009, A&A, 504, 73
Lawrence A., Elvis M., 2010, ApJ, 714, 561
Lyke B. W. et al., 2020, ApJS, 250, 8
Martínez-Sansigre A., Rawlings S., Lacy M., Fadda D., Marleau F. R., Simpson C., Willott C. J., Jarvis M. J., 2005, Nature, 436, 666
Martínez-Sansigre A., Rawlings S., Lacy M., Fadda D., Jarvis M. J., Marleau F. R., Simpson C., Willott C. J., 2006, MNRAS, 370, 1479
Matthee J. et al., 2024, ApJ, 963, 129
Mazzolari G. et al., 2025, A&A, 700, A12
Merloni A. et al., 2014, MNRAS, 437, 3550
Morrissey P. et al., 2018, ApJ, 864, 93
Netzer H., Wills B. J., Wills D., 1982, ApJ, 254, 489
Oke J. B. et al., 1995, PASP, 107, 375
Osterbrock D. E., Ferland G. J., 2006, Astrophysics of Gaseous Nebulae and Active Galactic Nuclei, 2nd edn. University Science Books, CA
Peca A. et al., 2023, ApJ, 943, 162
Peca A. et al., 2024, ApJ, 974, 156
Perrotta S., Hamann F., Zakamska N. L., Alexandroff R. M., Rupke D., Wylezalek D., 2019, MNRAS, 488, 4126
Pizzati E. et al., 2024, MNRAS, 534, 3155
Polletta M., Weedman D., Hönig S., Lonsdale C. J., Smith H. E., Houck J., 2008, ApJ, 675, 960
Polletta M. d. C. et al., 2006, ApJ, 642, 673
Prochaska J. et al., 2020, J. Open Source Softw., 5, 2308
Reyes R. et al., 2008, AJ, 136, 2373
Richards G. T. et al., 2006, AJ, 131, 2766
Ross N. P. et al., 2013, ApJ, 773, 14
Ross N. P. et al., 2015, MNRAS, 453, 3932
Sanders D. B., Soifer B. T., Elias J. H., Madore B. F., Matthews K., Neugebauer G., Scoville N. Z., 1988, ApJ, 325, 74
Schmidt M., 1963, Nature, 197, 1040
Schneider D. P. et al., 2007, AJ, 134, 102
Soltan A., 1982, MNRAS, 200, 115
Stalevski M., Ricci C., Ueda Y., Lira P., Fritz J., Baes M., 2016, MNRAS, 458, 2288
Stern D. et al., 2005, ApJ, 631, 163
Stern J., Laor A., 2012, MNRAS, 426, 2703
Temple M. J., Banerji M., Hewett P. C., Coatman L., Maddox N., Peroux C., 2019, MNRAS, 487, 2594
Tsai C.-W. et al., 2015, ApJ, 805, 90
Urry C. M., Padovani P., 1995, PASP, 107, 803
Villar Martín M., Perna M., Humphrey A., Castro Rodríguez N., Binette L., Pérez González P. G., Mateos S., Cabrera Lavers A., 2020, A&A, 634, A116
Wang B. et al., 2025, MNRAS, 539, 1562
Wang F. et al., 2021, ApJ, 907, L1
Wu J. et al., 2012, ApJ, 756, 96
Yan L. et al., 2013, AJ, 145, 55
Yuan S., Strauss M. A., Zakamska N. L., 2016, MNRAS, 462, 1603
Zakamska N. L., Alexandroff R. M., 2023, MNRAS, 525, 2716
Zakamska N. L. et al., 2003, AJ, 126, 2125
Zakamska N. L. et al., 2006, AJ, 132, 1496
Zakamska N. L. et al., 2016, MNRAS, 459, 3144
Zhang S. et al., 2023, Science, 380, 494
Zhou H., Wang T., Yuan W., Lu H., Dong X., Wang J., Lu Y., 2006, ApJS, 166, 128

APPENDIX A: GEMINI AND KECK SPECTRA FOR ALL THE TARGETS

Here we show the Gemini and Keck spectra for the rest of the targets. Targets with both Keck and Gemini spectra are shown in Figs A1, A2, A3, A4, A5, and A6. The four targets with Gemini spectra only are shown in Fig. A7.

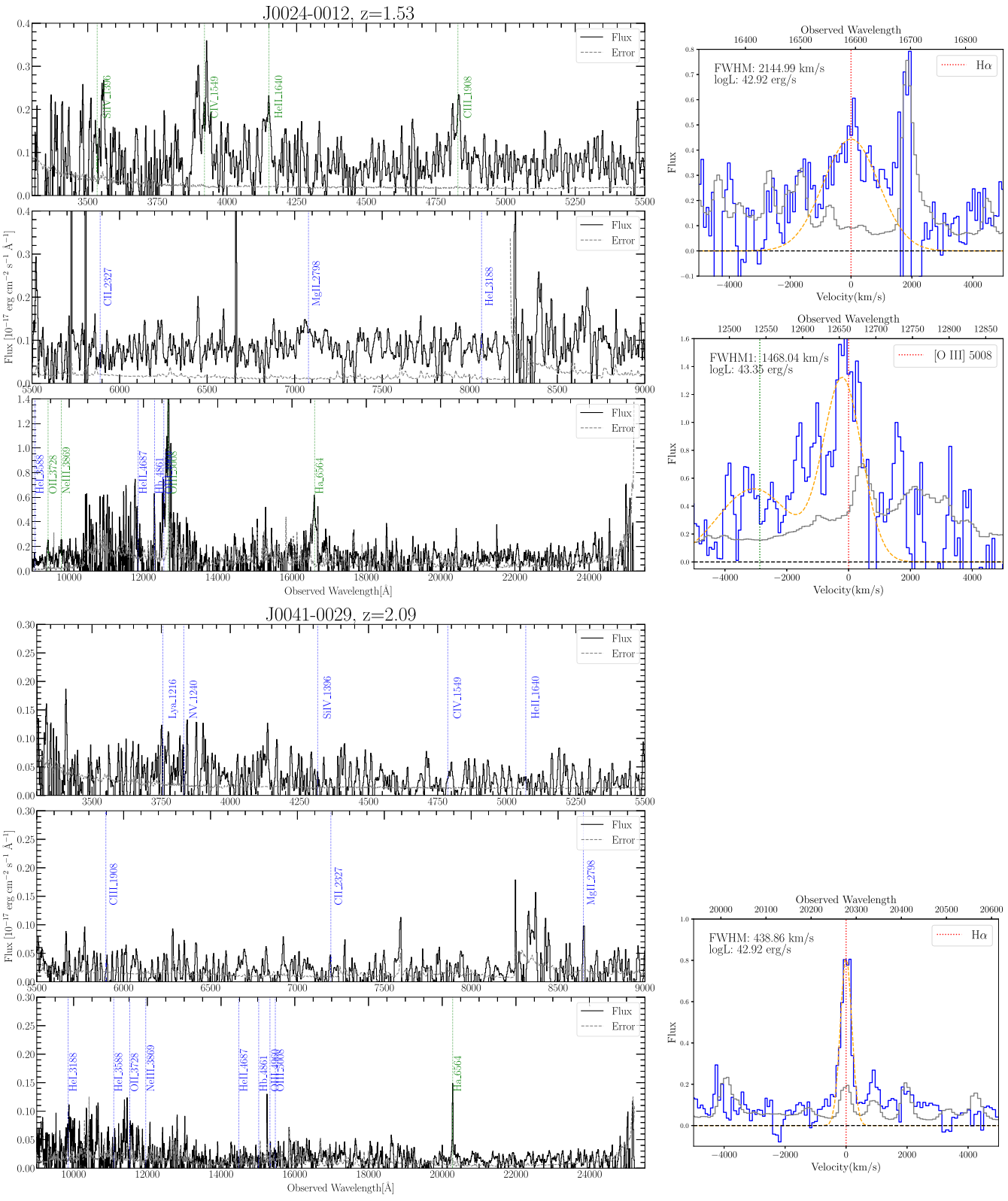

Figure A1. Reduced spectra and the fitted emission line for all our targets. Each left panel shows the coadded spectra from Keck and Gemini into three windows for better visibility. The dashed blue lines show the expected location of typical emission lines, and the dashed green lines show the detected lines. The right panel shows the fitting for Ly α, H α or [O III] emissions. The red dashed line shows the center of the emission line and the orange shows the Gaussian fitting.

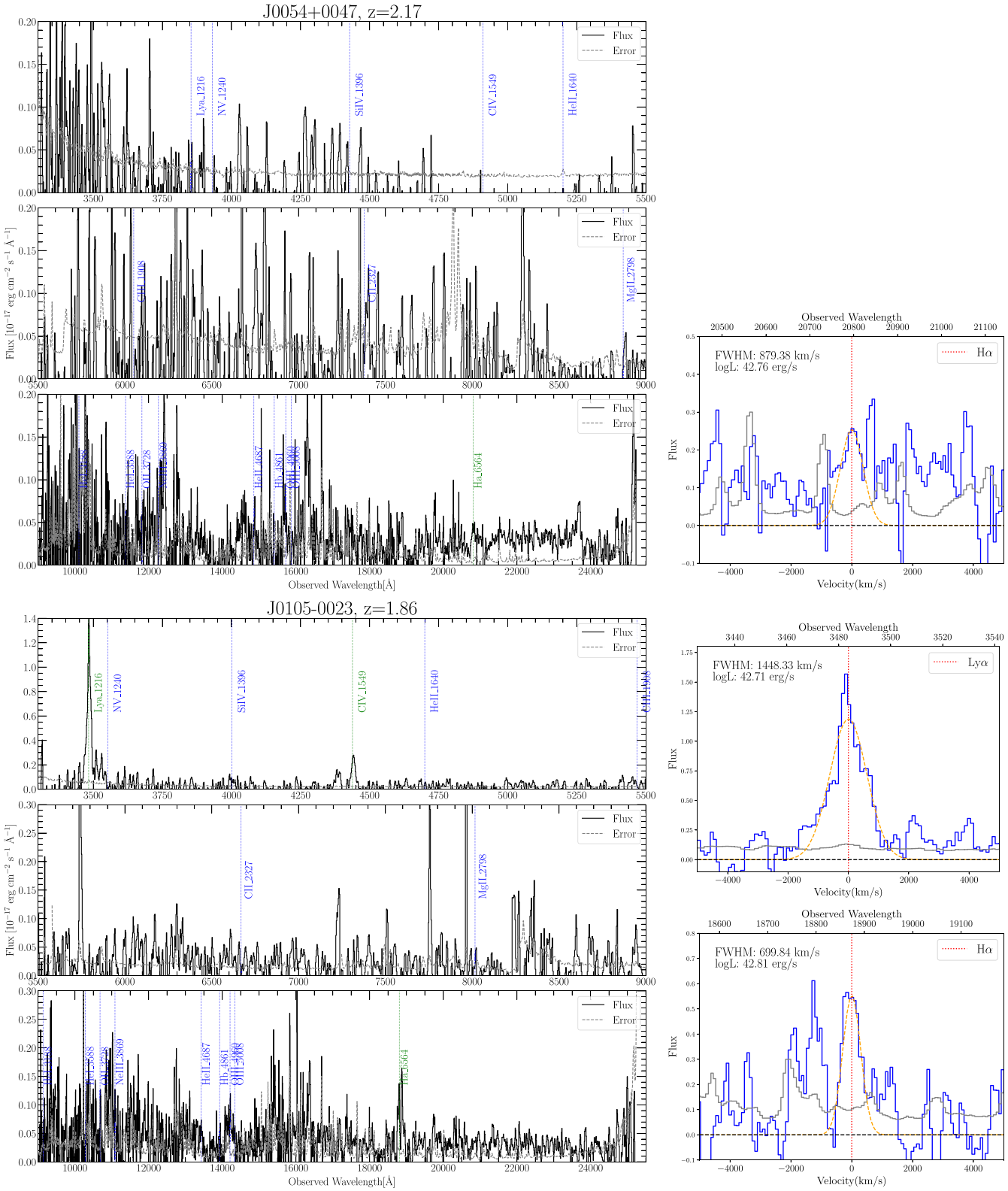

Figure A2. Spectra and line fittings for two targets in our sample.

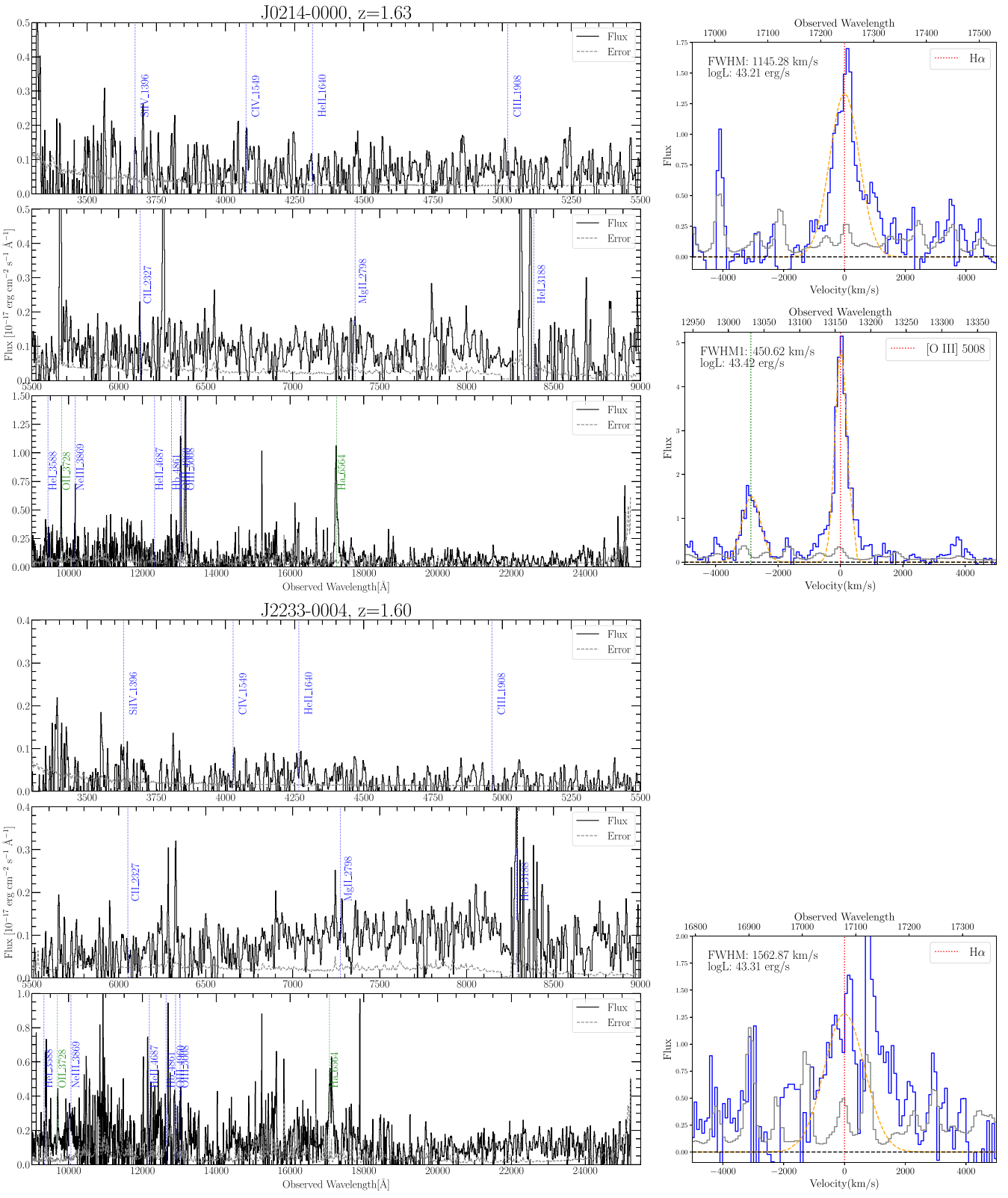

Figure A3. Spectra and line fittings for two targets in our sample.

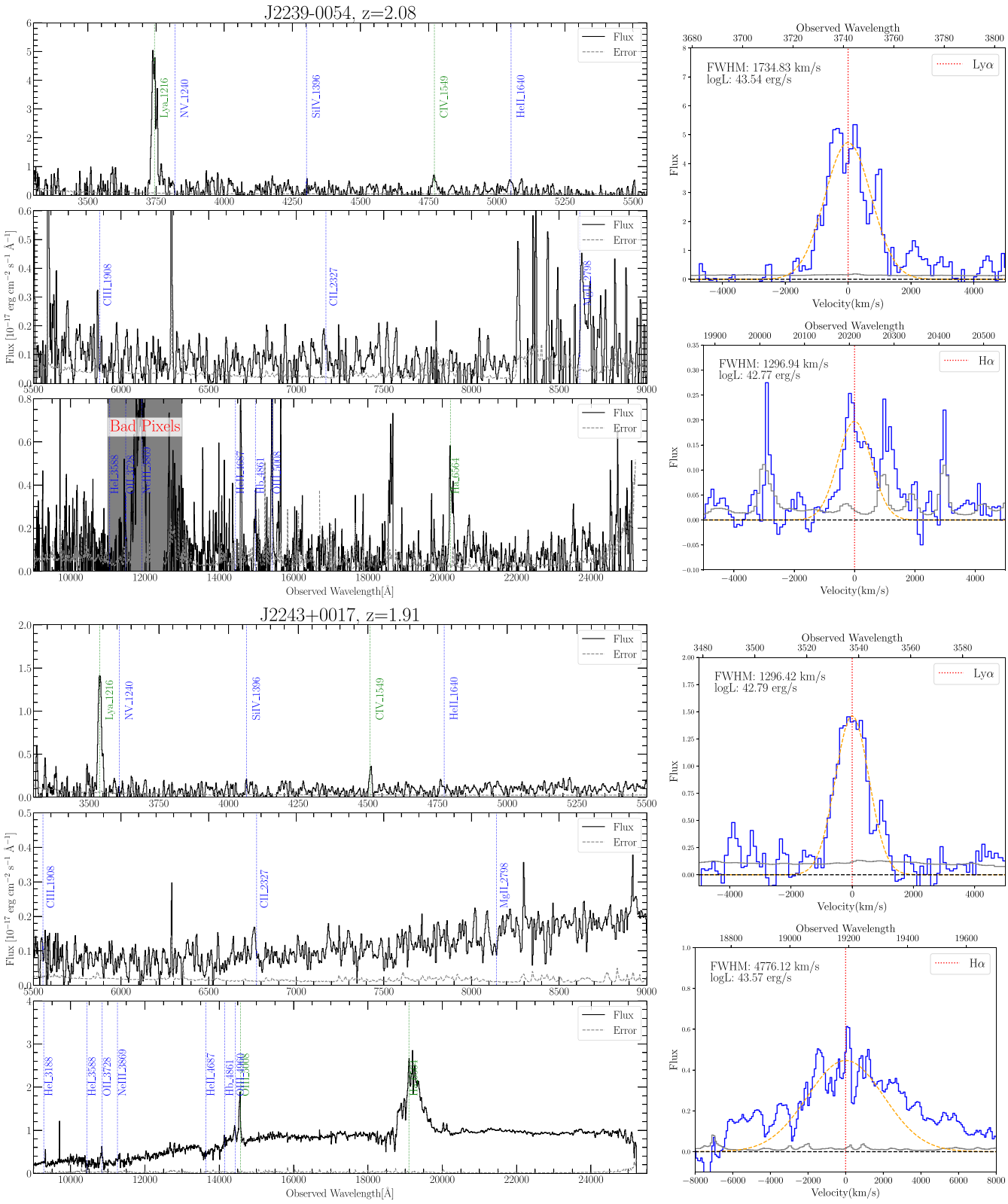

Figure A4. Spectra and line fittings for two targets in our sample.

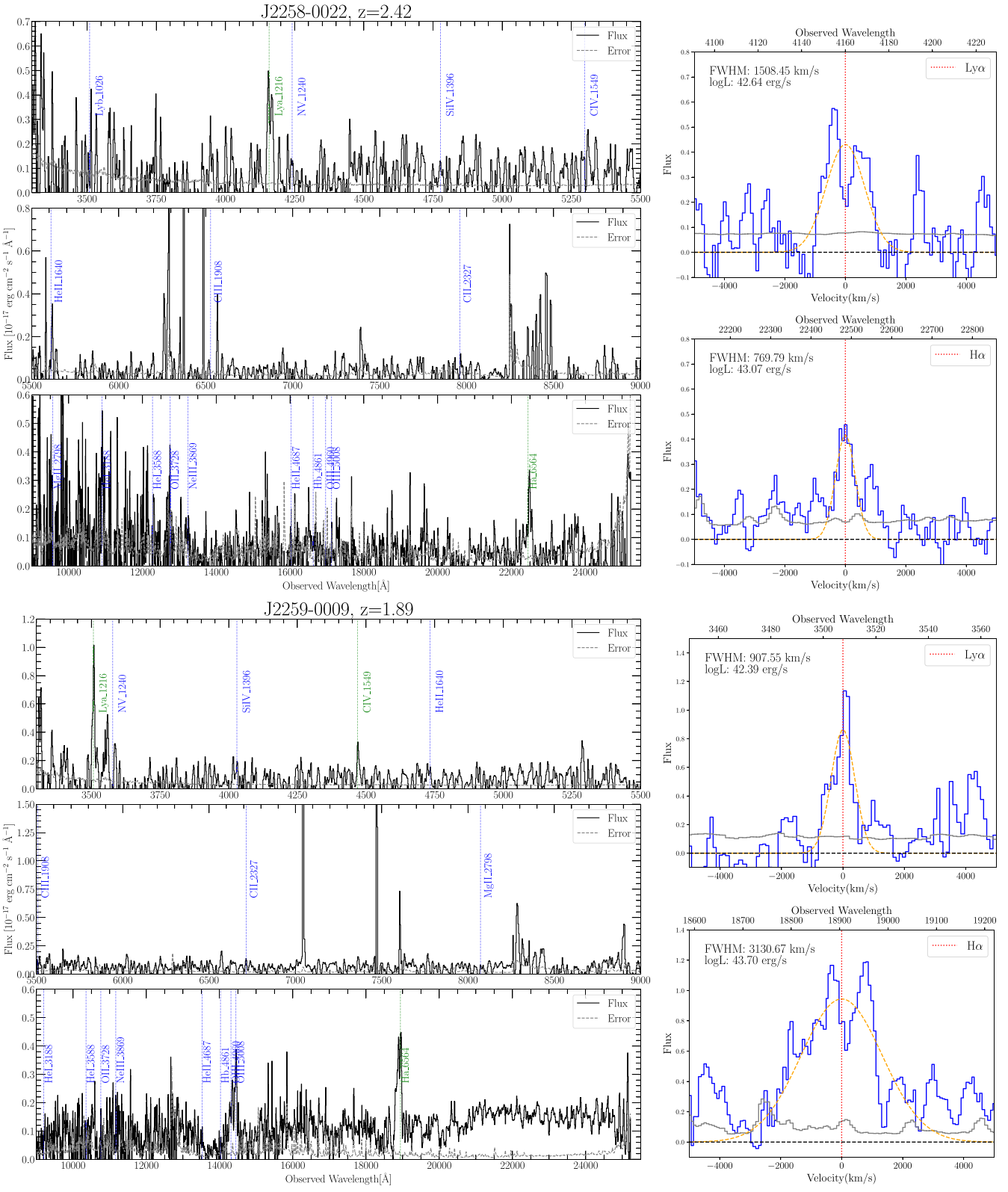

Figure A5. Spectra and line fittings for two targets in our sample.

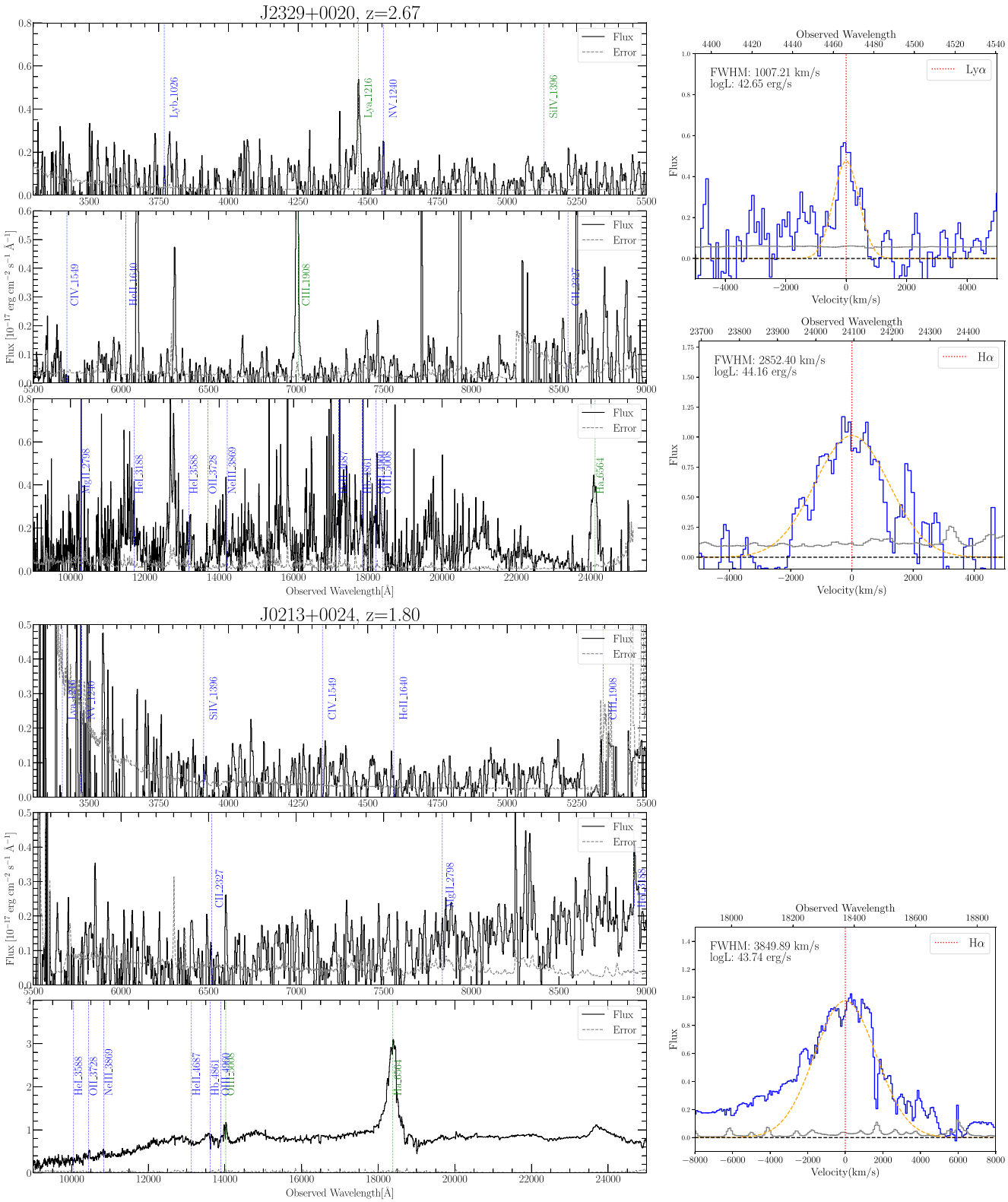

Figure A6. Spectra and line fittings for all the targets in our sample.

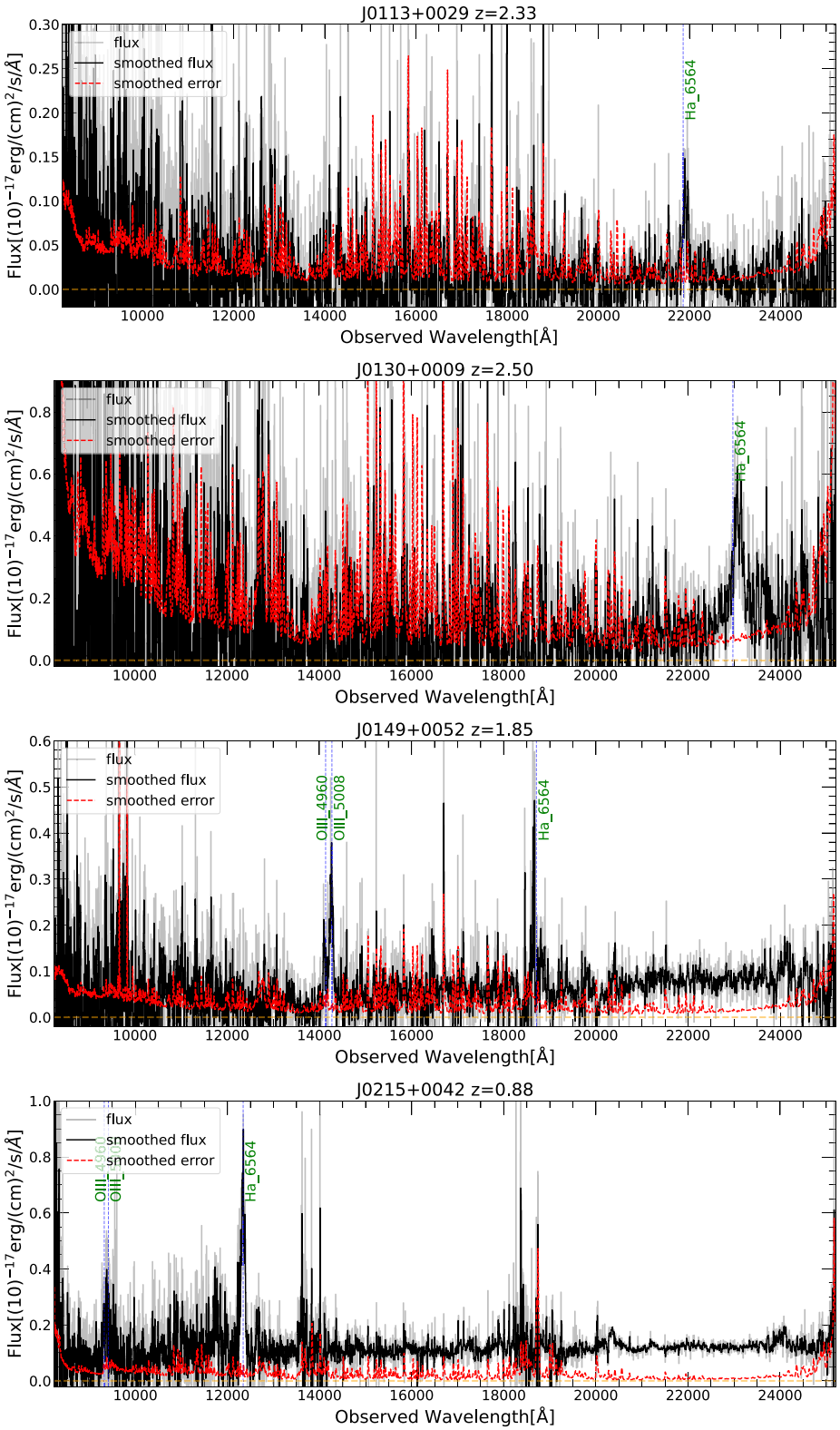

Figure A7. Four targets in our sample with Gemini/GNIRS spectra only.

This paper has been typeset from a TEX/LATEX file prepared by the author.